Anomalously large anisotropic magnetoresistance in a perovskite manganite

Run-Wei Li[a,b], Huabing Wang[b], Xuewen Wang[c], X. Z. Yu[b], Y. Matsui[b], Zhao-Hua Cheng[d], Bao-Gen Shen[d], E. Ward Plummer[e,1], and Jiandi Zhang[e,1]

[a]Ningbo Institute of Materials Technology and Engineering, Chinese Academy of Sciences, Ningbo, Zhejiang 315201, People's Republic of China; [b]National Institute for Materials Science (NIMS), Tsukuba, Ibaraki 305-0047, Japan; [c]Department of Physics, Florida International University, Miami, FL 33199; [d]Beijing National Laboratory for Condensed Matter Physics and Institute of Physics, Chinese Academy of Sciences, Beijing 100190, People's Republic of China; and [e]Department of Physics and Astronomy, Louisiana State University, Baton Rouge, LA 70803

Contributed by E. Ward Plummer, July 8, 2009 (sent for review November 28, 2008)

The signature of correlated electron materials (CEMs) is the coupling between spin, charge, orbital and lattice resulting in exotic functionality. This complexity is directly responsible for their tunability. We demonstrate here that the broken symmetry, through cubic to orthorhombic distortion in the lattice structure in a prototype manganite single crystal, $La_{0.69}Ca_{0.31}MnO_3$, leads to an anisotropic magneto-elastic response to an external field, and consequently to remarkable magneto-transport behavior. An anomalous anisotropic magnetoresistance (AMR) effect occurs close to the metal-insulator transition (MIT) in the system, showing a direct correlation with the anisotropic field-tuned MIT in the system and can be understood by means of a simple phenomenological model. A small crystalline anisotropy stimulates a ''colossal'' AMR near the MIT phase boundary of the system, thus revealing the intimate interplay between magneto- and electronic-crystalline couplings.

metal-insulator transition | CEM

The striking transport properties of many CEMs, such as unconventional superconductivity and ''colossal'' magnetoresistance (CMR), are believed to be manifested by a coexistence of a variety of complex interactions that couple simultaneously active degrees of freedom (1). Consequently, such complex couplings lead to multifunctionalities displayed by these materials. The hallmark of these materials is the multitude of competing ground states that can be tuned or manipulated by doping, structural manipulations, strain induction, or the application of external stimulus, such as pressure, electric or magnetic fields. In doped manganites $Ln_{1-x}A_xMnO_3$ where Ln and A are rare- and alkaline-earth cations, respectively, ferromagnetic (FM) metallic, paramagnetic (PM) insulating and antiferromagnetic (AF) charge/orbital ordered states are among these competing ground states (2). External fields influence the subtle balance of the interactions and induce phase transitions between different ground states (3–5). Examples include the CMR and giant anisotropic magnetoresistance (AMR) effects in which the transport has ''colossal'' response to an external field, thus offering intriguing opportunities for new technological applications with advanced correlated electron devices (6).

Magnetoresistance (MR) is a property of materials in which the resistivity depends on the strength of applied magnetic field. Anisotropic magnetoresistance (7), on the other hand, is when the resistivity also depends on the field orientation with respect to either the electrical current or the crystal axes. Whereas the dependence of resistivity on the field direction relative to the electrical current, known as ordinary MR or Lorentzian MR, is expected due to the Lorentz force acting on the conduction electrons; the dependence of resistivity on the field orientation with respect to the crystal axes is much more unusual. However, this kind of AMR provides detailed information about the underlying physics such as spin-orbital and magneto-elastic couplings in a material and it also enables wide range of technological applications. The most prominent technological application of giant MR is in the data storage industry. Yet, the advantage of AMR over conventional MR is that AMR can be applied for sensor of field direction and dimensional imaging.

AMR effects are small in most of FM metals and alloys (8), typically with a magnitude of few percent. Recently, it was discovered that giant and unusual AMR effects with a magnitude of $>30\%$ exist in several perovskite manganite thin films (9–14). Particularly, the observed AMR exhibits strong and nonmonotonic temperature (T) (11–14) and field (H) dependence (9, 14). This kind of behavior differs dramatically from what has been observed in conventional 3*d* transition metals or alloys, suggesting a different mechanism beyond conventional theories of AMR. For example, the AMR amplitude in $La_{0.7}Ca_{0.3}MnO_3$ films (10, 11, 13) and in the strained $Pr_{0.67}Sr_{0.33}MnO_3$ films (12) shows a giant enhancement near the Curie temperature or metal-insulator transition (MIT) temperature (T_{MI}), whereas conventional AMR in 3*d* transition metals or alloys depends monotonically on temperature. Furthermore, the sign of the AMR can be tuned from negative to positive by inducing lattice strain to the films through the lattice mismatch between the films and substrate, indicating a strong influence of lattice distortion (12). Most studies of the AMR have focused on thin films. Many extrinsic effects, including the substrate-induced strain and the large demagnetization field due to the large apical ratio in film geometry, have impeded thorough investigations of the inherent nature of AMR in this class of CEMs. In particular, it is unclear whether the observed giant AMR effect is truly intrinsic due to magneto-elastic or spin-orbital couplings. If indeed this is the case, then how does one understand the unusual temperature and field dependence of observed AMR? Why does the AMR always have its maximum value near T_{MI}? Here, we have taken a different approach by systematically investigating the single crystals of $La_{1-x}Ca_xMnO_3$ ($x \sim 0.31$). Our results on magneto transport clearly show that the observed anomalous AMR has an intimate relationship with the crystalline anisotropy in the system. We provide a phenomenological model to explain the observed phenomena, which should be also applicable to other CEMs with strong magneto-elastic coupling.

$La_{1-x}Ca_xMnO_3$ ($x \sim 0.31$) single crystals are orthorhombic, deviating from the cubic perovskite structure via two dissimilar Jahn-Teller (*J–T*) distortions—in-plane (i.e., in ***ab***-plane) rotation and out-of-plane (***c***-axis) tilt of the MnO_6 octahedron (15, 16). A MIT coincides with a FM-to-PM transition at $T_{MI} \cong 220$

Author contributions: R.-W.L., H.W., and J.Z. designed research; R.-W.L., H.W., X.Z.Y., Y.M., Z.-H.C., and B.-G.S. performed research; R.-W.L., H.W., X.W., X.Z.Y., Y.M., B.-G.S., E.W.P., and J.Z. analyzed data; and R.-W.L., E.W.P., and J.Z. wrote the paper.

The authors declare no conflict of interest.

Freely available online through the PNAS open access option.

[1]To whom correspondence may be addressed. E-mail: jiandiz@lsu.edu or wplummer@lsu.edu.

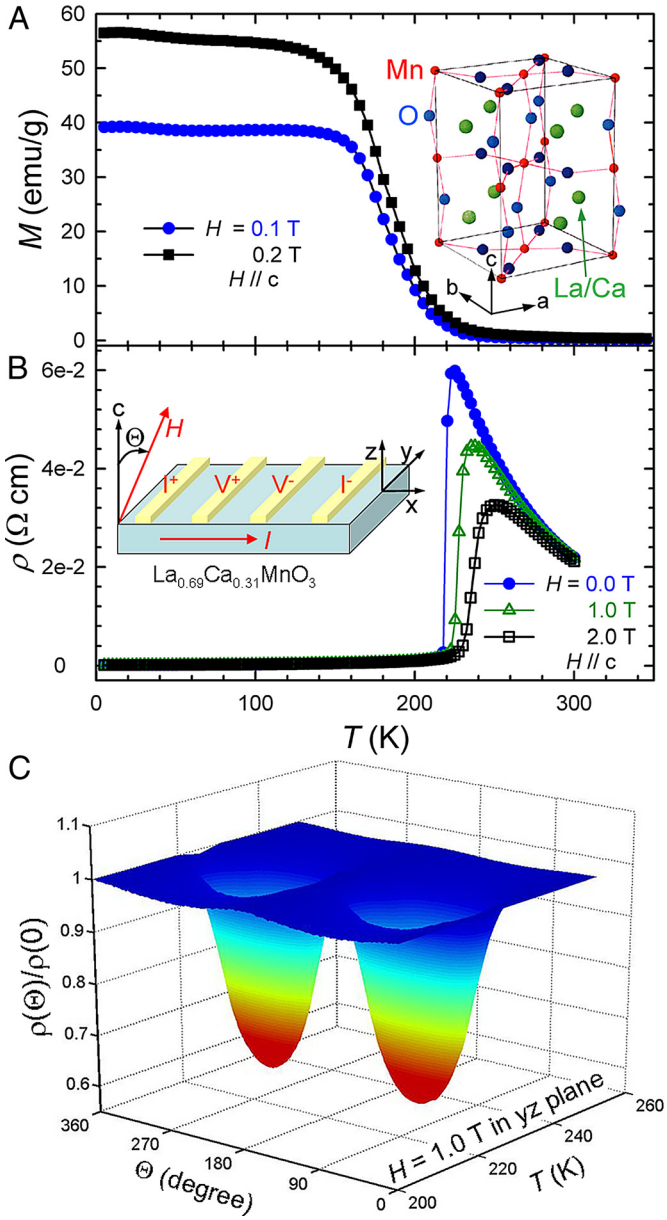

Fig. 1. Magnetic and magneto-transport properties of $La_{0.69}Ca_{0.31}MnO_3$. (*A*) *T*-dependence of the magnetization with an *Inset* showing the unit cell structure as well as the crystalline axes. (*B*) *T*-dependence of the resistivity measured from a slab of a single crystal under different fields. The *Inset* shows a schematic arrangement of the measurements from the crystal with a slab sample size: 3.8 × 0.85 × 0.15 mm^3. The sample *c*-axis is normal to the slab plane. (*C*) Angle- and *T*-dependences of the normalized resistivity, $\rho(\Theta)/\rho(\Theta) = 0°$, measured under a magnetic field rotating about the *x*-direction (i.e., the current (*I*) direction).

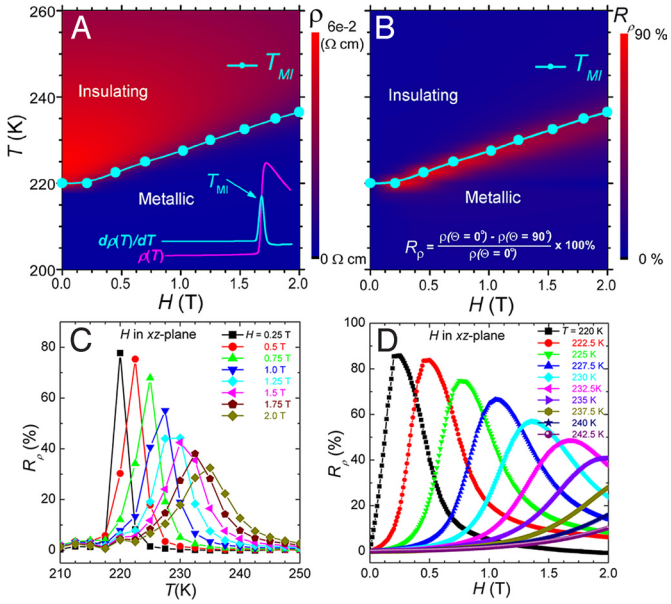

Fig. 2. Correlation between MIT and AMR of $La_{0.69}Ca_{0.31}MnO_3$. (*A*) *T*- and *H*-(along *c*-axis) dependence of the resistivity (ρ) and T_{MI} defined as the peak temperature in $d\rho/dT - T$ curve (see the *Inset*). (*B*) A contour plot and line plots of (*C*) the *T*- and (*D*) *H*-dependence of the measured R_ρ from the slab single crystal as the field was applied in the *xz* plane (thus including Lorentzian MR). The solid lines through the data points are guides to the eye.

K, characterized by the *T*-dependence of magnetization $M(T)$ and the resistivity $\rho(T)$ shown in Fig. 1 *A* and *B*, respectively. The measured $\rho(T)$ vs. $\boldsymbol{H}$ curve demonstrates a typical negative magnetoresistance behavior. However, the observed MR shows a strong dependence on the field orientation, leading to a remarkable AMR effect.

We used a single crystal of a slab shape (shown in the *Inset* of Fig. 1*B*) where the $\boldsymbol{c}$-axis is perpendicular to the slab plane (*xy* plane). Fig. 1*C* shows $\rho(T,\Theta)$ under a $\boldsymbol{H} = 1.0$ T field rotating in the *yz* plane with angle Θ between the field and $\boldsymbol{c}$-axis, which demonstrates a strong *T*-dependence of the AMR effect with the peak value achieved very close to T_{MI}. The AMR amplitude is defined as $R_\rho \equiv (1 - \rho_\perp/\rho_{//}) \times 100\%$, where $\rho_{//} \equiv \rho(\Theta = 0)$ and $\rho_\perp \equiv \rho(\Theta = 90°)$ are the resistivities for a given field being parallel and perpendicular to the $\boldsymbol{c}$-axis of the crystal, respectively. For $\boldsymbol{H} = 1.0$ T, a peak value of $R_\rho \sim 40\%$ is observed near T_{MI}. In this case, the measurement contains no contribution of the conventional Lorentzian MR because the field rotates in the plane perpendicular to the current direction. This anomalous *T*-dependent AMR must be related to the magneto-crystalline anisotropy and closely associated with the coupled MIT and FM-to-PM transition in the crystal.

We systematically investigated the temperature- and field-dependence of AMR and their correlation with the field-dependent MIT. The results are shown in Fig. 2. T_{MI} increases almost linearly with field (see Fig. 2*A*). A key discovery here is that the measured R_ρ peak follows almost exactly the field-dependence of T_{MI}, as shown in Fig. 2*B*. Large AMR emerges only near T_{MI} (Fig. 2*C*), whereas no prominent AMR appears in either the pure FM-metallic state at $T \leq T_{MI}$ or the pure PM-insulating state at $T \geq T_{MI}$. Likewise, the nonmonotonic field-dependence of R_ρ at a given *T* close to T_{MI} is evident in Fig. 2*D*, such that $R_\rho(H$ and $T)$ exhibits very similar line shapes for varying field or temperature.

Fig. 3 presents the measured field-dependence of both the normalized resistivity and T_{MI} for the field along three different sample orientations. The measured $\rho(\boldsymbol{H})$ has similar values for the $\boldsymbol{H}//x$ and $\boldsymbol{H}//y$ directions but quite different values for the $\boldsymbol{H}//z$ direction (see Fig. 3*A*). A small difference in $\rho(\boldsymbol{H})$ between the $\boldsymbol{H}//x$ and $\boldsymbol{H}//y$ directions can mainly be attributed to the Lorentzian MR, whereas the large difference between the $\boldsymbol{H}//z$ and $\boldsymbol{H}//x(y)$ directions gives rise to the observed giant AMR. Also shown in the *Inset* of Fig. 3*B*, a small but clear shift of $\rho(T)$ is evident by orienting $\boldsymbol{H}//z$- from $\boldsymbol{H}//x(y)$-direction, thus indicating an anisotropic field-dependent MIT. As presented in Fig. 3*B*, the $T_{MI}(\boldsymbol{H})$ curve for the $\boldsymbol{H}//z$ direction deviates from that for the $\boldsymbol{H}//x(y)$ direction. The crystalline $\boldsymbol{c}$-axis (i.e., the *z* direction), which is perpendicular to the sample plane, is the hard axis for

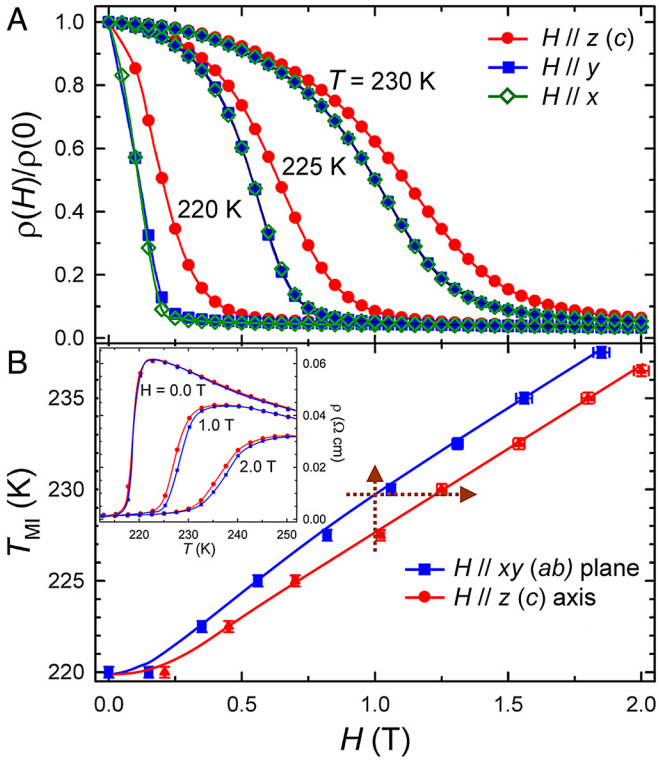

Fig. 3. Field-orientation dependence of magnetoresistance and MIT in $La_{0.69}Ca_{0.31}MnO_3$. (*A*) Field strength and orientation dependence of resistivity normalized to its zero-field value at the temperatures near T_{MI} and (*B*) T_{MI} measured from the slab single crystal (see the *Inset* of Fig. 1*B*). The *Inset* presents the *T*-dependence of resistivity on warming under different values of magnetic field along *z*(*c*)-axis (solid circle) and in *xy*(*ab*)-plane. The solid lines are guides to the eye. The dashed arrows indicate the horizontal and vertical cuts for a fixed temperature and field, respectively.

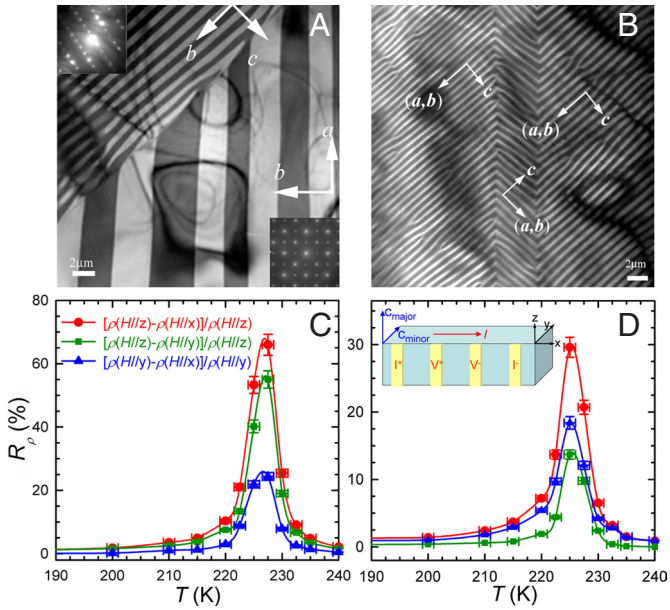

Fig. 4. Crystal twinning behavior of $La_{0.69}Ca_{0.31}MnO_3$. Lorentzian TEM images with the selected-area electron diffraction patterns of corresponding areas at $T = 80$ K with different crystalline orientations. (*A*) The 45° crystal twinning between *a*- and *b*-axis. (*B*) The 90° crystal twinning in the *c*-axis. The *T* dependence of the anisotropic R_ρ at $\boldsymbol{H} = 1.0$ T measured from (*C*) the slab and (*D*) a square-rod $La_{0.69}Ca_{0.31}MnO_3$ single crystal. The *Inset* shows a schematic arrangement of the measurements from the square-rod sample size: 7.0 × 0.85 × 0.85 mm^3. The *c*-axis is in the plane perpendicular to the current direction.

the field-dependent MIT. We conclude that the observed large AMR simply reflects the uniaxial magneto-crystalline anisotropy in the system.

The correlation between AMR and MIT displayed in Fig. 2 and Fig. 3, especially the gap of the two $T_{MI}(\boldsymbol{H})$ curves shown in Fig. 3*B*, provide a crucial key for understanding the anisotropic magneto-transport properties. The difference in T_{MI} due to field orientations ($\boldsymbol{H}$//$\boldsymbol{c}$- or $\boldsymbol{H}\perp\boldsymbol{c}$-axis) leads to the observed unusual AMR effect. At a given field strength (vertical cut and between the two T_{MI} curves in Fig. 3*B*), the sample becomes insulating when $\boldsymbol{H}$//$\boldsymbol{c}$-axis while remaining metallic when $\boldsymbol{H}\perp\boldsymbol{c}$-axis—creating the R_ρ peak as shown in Fig. 2*C*. On the other hand, at a given *T* (horizontal cut in Fig. 3*B*), the sample becomes metallic as $\boldsymbol{H}\perp\boldsymbol{c}$-axis but remains insulating as $\boldsymbol{H}$//$\boldsymbol{c}$-axis, thus resulting in the R_ρ peak as shown in Fig. 2*D*. When the system is far away from the gap region of the two $T_{MI}(\boldsymbol{H})$ curves, only conventional AMR with small amplitude should exist. Furthermore, increasing the field gradually reduces the R_ρ (see Fig. 2*D*). Thus, one can anticipate that the AMR effect as well as the anisotropy of field-dependent MIT (the gap in Fig. 3*B*) should vanish under a sufficiently strong field.

Jahn-Teller distortions (17) and double-exchange (DE) interactions (18, 19), which are intimately coupled in this class of doped oxides, play vital roles in both the transport and the magnetic properties. Simply speaking, Jahn–Teller (J-T) distortions tend to promote insulating phase to the system whereas DE interaction endorses FM metallic state, although the strength of DE interaction depends on the degrees of J-T distortions thus making a close coupling between them. Bending the Mn-O-Mn bond by enhancing J-T distortion reduces DE interaction so as bandwidth. The subtle competition between them causes the MIT in these doped manganites. However, external field tends to disturb such a competition by facilitating the metallic state, evident by appearing *negative* CMR near the T_{MI} and tuning the MIT (16, 20–22). Owning to the strong correlation character in these materials, lattice also has its response to applied magnetic field by alter J-T distortions, depending on the detailed lattice structure and applied field orientation. One possible lattice response is a suppression of J-T distortions by straightening the Mn-O-Mn bond thus causes negative CMR by enhancing DE interactions. Indeed, the giant AMR observed in $La_{1-x}Ca_xMnO_3$ reflects exactly the different lattice response to the external field, depending on the field direction.

If, in a cubic peroviskite structure, lattice should have identical response to external field in all high-symmetry crystalline directions, thus no AMR is generated by magneto-elastic coupling. However, in orthorhombic $La_{1-x}Ca_xMnO_3$, the structure has lower symmetry by bearing two distinct J-T distortions from a cubic perovskite. The lattice has larger response when the field is perpendicular to $\boldsymbol{c}$-axis than parallel to $\boldsymbol{c}$-axis, thus creating distinct effects on the transport properties including MIT through different couplings with the DE interaction. This different response exactly makes $\boldsymbol{c}$-axis as the hard axis for the field-dependent MIT, having a small but crucial anisotropy as clearly shown in the two field-dependent T_{MI} curves (see Fig. 3*B*). Consequently, the system exhibits a giant AMR effect near the MIT region that is stimulated by the distinct lattice response to external field because of the asymmetric J-T distortions.

Based upon the above scenario for the nature of intrinsic AMR, we are able to qualitatively explain the dissimilar magnitude of AMR effects observed in different manganite systems (9–14). Because the AMR effect depends on the dissimilar response of J-T lattice distortions to external field, a system

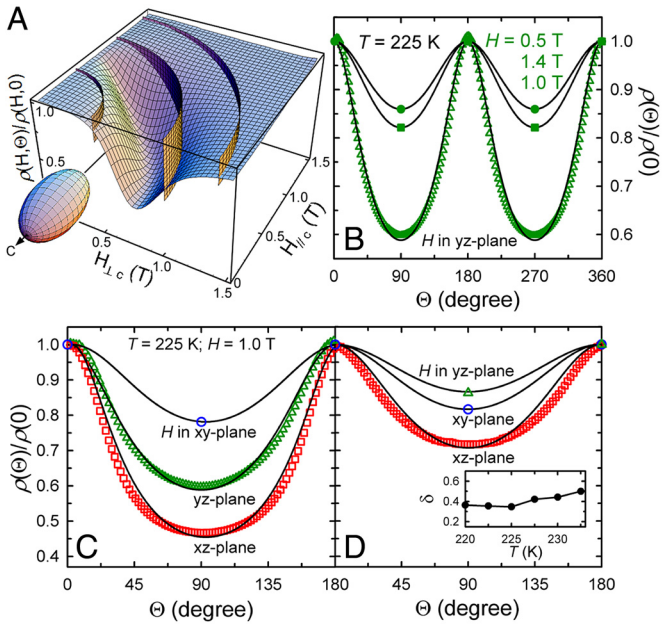

Fig. 5. Phenomenological uniaxial anisotropy model for the AMR of $La_{0.69}Ca_{0.31}MnO_3$. (*A*) Calculated normalized resistivity at a given temperature as a function of magnetic field strength and orientation with respect to the crystal *c*-axis (Θ), based upon the uniaxial anisotropic model (see the *Inset* for the uniaxial resistivity ellipsoid). (*B*) Calculated (solid lines) Θ-dependence of normalized resistivity for three values of fields (corresponding to the three sheets in *A*) rotating in the *yz* plane, compared with the experimental results (symbols) measured from the slab sample at $T = 225$ K. (*C* and *D*) Calculated angle dependence of normalized resistivity for a field of $H = 1.0$ T rotating in three perpendicular planes (from *y* to *x*, *z* to *y*, and *z* to *x* direction), compared with the experimental results (symbols) measured at $T = 225$ K from the slab (see Fig. 1) and square-rod (see Fig. 4.) sample, respectively.

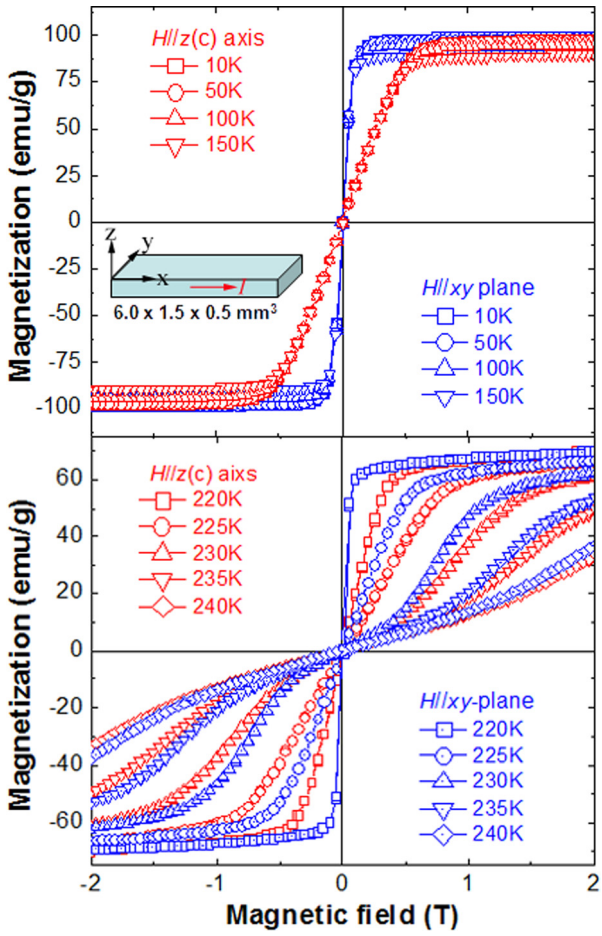

Fig. 6. The magnetization of $La_{0.69}Ca_{0.31}MnO_3$ as a function of magnetic field for the two distinct field directions measured at different temperature, $H//z(c)$- and $H\perp z(c)$-axis, respectively.

with stronger J-T distortions should have greater AMR effect. This mechanism explains that, in a similar doping level of $x \sim 0.3$, $La_{1-x}Sr_xMnO_3$ (14) has a smaller AMR effect than $Pr_{1-x}Sr_xMnO_3$ (12) and $La_{1-x}Ca_xMnO_3$ (9–11, 13) simply because of fewer J-T distortions.

Because the intrinsic AMR discussed above is closely related to crystalline orientation, twinning in a single crystal could dramatically affect the characterization of AMR properties. Imagine that a single crystal is randomly and completely twinned, then, the intrinsic AMR related to crystalline anisotropy would be averaged out. In such a case, a possible AMR would only be the result of the demagnetization field effects because of the geometric shape of the slab sample. However, we believe that this is not the case. First, demagnetization field effects cannot generate such large amplitude of AMR. More importantly, any demagnetization effect cannot result in the unusual field- and temperature-dependence of AMR as observed in the system.

To further explore the issue arising from the twinning and demagnetization field effect, we have investigated the possible twinning domain structure in the system. Fig. 4 *A* and *B* presents two Lorentzian TEM images with selected-area electron diffraction patterns of the corresponding domain areas. The images reveal magnetic domain structure, thus reflecting crystalline twinning domain structure (23). Two distinct twinning cases are revealed. The twinning between the ***a***- and ***b***-axis, or in-plane twinning, is found via a 45° (or 135°) rotation of each other (Fig. 4*A*); whereas the twinning between the ***a***- (or ***b***-) and ***c***-axis, or out-of-plane twinning, is found through a 90° rotation of each other (Fig. 4*B*). It is expected that in-plane twinning is more common than out-of-plane twinning in orthorhombic crystals. Both the small MR difference between the $\boldsymbol{H}//x$ and $\boldsymbol{H}//y$ directions (Fig. 3*A*) and relatively small R_ρ as the field rotates in the *xy* plane (Fig. 4*C*) indicate that the twinning existing in the slab sample is mainly the in-plane type.

To corroborate this uniaxial anisotropy scenario, we have repeated the AMR measurements on a square-rod sample that, because of the increased size of the sample in the *z* direction, is anticipated to display more out-of-plane twinning and smaller demagnetization field than the slab sample. The results are shown in Fig. 4*D*. Compared with the results obtained from the slab sample, the R_ρ values, as the field rotates in the *xz* (red curve) and *yz* plane (green curve), are substantially suppressed in the square-rod sample. Furthermore, the order in the magnitude of R_ρ curves (green and blue) between the field rotating in the *yz* and *xy* planes is also switched. These results are exactly as expected because of the substantial out-of-plane twinning existing in the square-rod sample—portions of the crystal domain have their hard-axis (***c***-axis) oriented in the *y* direction (or *x* direction). Such a mixture of hard-axis orientation should suppress the intrinsic uniaxial anisotropy. Because there is a component of hard axis in the *y* direction, the R_ρ in the *xy* plane is enhanced, whereas that in the *yz* plane is reduced, resulting in the order switch of R_ρ curves.

The observed results can be quantitatively explained by a phenomenological model with a uniaxial AMR caused by the crystalline anisotropy. We start with the description of the model and then explain the data from both slab and square-rod

PHYSICS

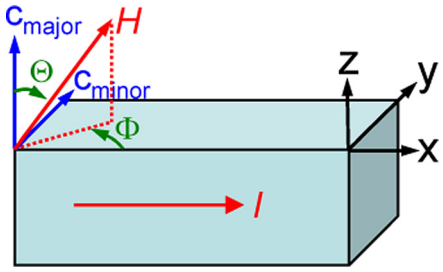

Fig. 7. Schematic view of the relative orientation relation between magnetic field (*H*), measured current (*I*), and crystal axis of square-rod sample existing two *c*-axis components due to twinning domains.

samples. Assuming the resistivities for a given field parallel and perpendicular to the ***c***-axis of the crystal are $\rho_{//}$ and $\rho_{\perp}$, respectively, a uniaxial resistivity ellipsoid (a prolate if $\rho_{//} \geq \rho_{\perp}$) can be constructed through the equation

$$\left(\frac{\rho(\Theta)}{\rho_{//}}\right)^2 \cos^2\Theta + \left(\frac{\rho(\Theta)}{\rho_{\perp}}\right)^2 \sin^2\Theta = 1, \qquad [1]$$

as is shown in Fig. 5*A*, where the short-to-long axial ratio representing the uniaxial resistivity ratio is $\alpha \equiv \rho_{\perp}/\rho_{//}$. The normalized resistivity $\rho(\Theta)/\rho_{//}$ can be expressed as

$$\frac{\rho(\Theta)}{\rho_{//}} = \alpha(\alpha^2 \cos^2\Theta + \sin^2\Theta)^{-1/2}. \qquad [2]$$

AMR is completely determined by the ratio α. If the anisotropy is relatively weak, i.e., $\alpha \approx 1$, the normalized resistivity can be approximately expressed as

$$\frac{\rho(\Theta)}{\rho_{//}} \cong \cos^2\Theta + \alpha\sin^2\Theta \qquad [3]$$

that is described as a symmetric sinusoidal function of the angle Θ.

In conventional materials, uniaxial AMR is relatively small ($R_\rho < 10\%$), weakly dependent on field and temperature, and can be described well with Eq. **3**. However, as shown in Fig. 2 *C* and *D*, the R_ρ in $La_{1-x}Ca_xMnO_3$ shows very strong *T*- and ***H***-dependence, i.e., $\alpha = \alpha(T,\boldsymbol{H})$. Furthermore, as shown in Fig. 5*B*, the $\rho(\Theta)/\rho$ (0) curve deviates greatly from the symmetric sinusoidal function depicted by Eq. **3**. Thus, we used Eq. **2** to reproduce the measured data. For *T* close to T_{MI}, a normalized $\rho(\boldsymbol{H},\Theta)/\rho(\boldsymbol{H},\Theta = 0)$ or $\rho(\boldsymbol{H}_{//},\boldsymbol{H}_{\perp})/\rho(\boldsymbol{H},\Theta = 0)$ is calculated and shown in Fig. 5*A* as a curved 3D MR sheet, where $\boldsymbol{H}_{//} = \boldsymbol{H}\cos\Theta$ and $\boldsymbol{H}_{\perp} = \boldsymbol{H}\sin\Theta$, respectively. The only fitting parameter here is $\alpha(\boldsymbol{H})$ at a given *T*.* For a given ***H***, the cross section between the MR sheet and a particular vertical ***H*** sheet reveals a normalized $\rho(\Theta)/\rho(0)$. Fig. 5*B* presents the calculated and measured $\rho(\Theta)/\rho(0)$ from the slab sample for the three ***H*** values at $T = 225$ K and as ***H*** rotates in the *yz* plane. We obtain $\alpha = 0.598$ for $\boldsymbol{H} = 1.0$ T and $T = 225$ K.

As shown in Fig. 5*B* and Fig. 1*C*, the line shape of $\rho(\Theta)/\rho(0)$ clearly shows a peak-to-valley asymmetry with a larger valley width, in contrast with the symmetric line shape given by Eq. **3**. The excellent agreement between theoretical and experimental results in Fig. 5*B* along with an evidently large asymmetric line shape provides the justification for Eq. **2**. It is noteworthy that films of $Pr_{2/3}Sr_{1/3}MnO_3$ with large AMR also exhibit similar asymmetry $\rho(\Theta)/\rho(0)$ shape (12).

*For simplification, here we neglect the contribution of Lorentzian MR and sample shape-induced demagnetization effects. There will be more parameters if these factors are considered.

The phenomenological model can reproduce all of the experimental AMR data for field rotation in different sample planes for both slab and square-rod samples. Fig. 5*C* shows both theoretical and experimental results with excellent agreement for the slab sample. For the square-rod sample (see Fig. 4*D*), the measured R_ρ is much smaller than that of the slab sample, mainly because of the substantial ***c***-axis mixture in the *yz* plane (see *Inset* in Fig. 4*D*). Therefore, we propose a two-component model (see *Methods*). Each component satisfies Eq. **2** and has the same α value as the slab sample. The only additional parameter introduced here is the twinning portion parameter (δ): the amount of the minor ***c***-axis component ($\delta \leq 0.5$). This single parameter δ is fitted with the $\rho(\Theta)/\rho(0)$ data from the square-rod sample, and the results are shown in Fig. 5*D*. The agreement between the theoretical results and experimental data are very impressive, considering that we neglect other contributions such as the Lorentzian MR. As shown in the *Inset* of Fig. 5*D*, a quite reasonable value of $\delta \sim 0.40$ is obtained, and it remains reasonably constant at different temperatures, further confirming the validity of the model.

Methods

Experimental. $La_{0.69}Ca_{0.31}MnO_3$ single crystals were grown using the traveling solvent optical floating zone technique. Samples of both the slab and square-rod shapes for the measurements were cut from the same single-crystal rod such that the *x* direction was almost along the crystal rod growing direction. There is a slightly offset in the doping concentration such that the measure $T_{MI} \sim 220$ K is lower than the published value of $T_{MI} \sim 250$ K. The crystal orientation of the samples was carefully examined by X-ray diffraction. The *T*-dependence of the magnetization was measured by a superconducting quantum interference device magnetometer (SQUID, Quantum Design). The MR measurements were carried out using a Physical Property Measuring System (PPMS, Quantum Design) equipped with a motorized sample rotator. The standard four-probe method was used for the resistivity measurements. The angular dependence of the resistivity $\rho(\Theta)$ was measured at a fixed magnetic field and temperature by varying the sample orientation relative to the field. To avoid Joule heating effects, a measuring electrical current was used below 100 μA in all of the electrical measurements. To ensure that the observed AMR is not just simply caused by a magnetization anisotropy, we have measured the magnetization as a function of magnetic field for the two distinct field directions, ***H***//*z*(***c***)- and ***H***$\perp$*z*(***c***)-axis, respectively. The result is shown in Fig. 6 for the measured magnetization curves at different temperatures. The magnetization anisotropy with hard magnetic axis in **c**-axis direction exists in the low field case; the saturation field is only ~0.5 T in the FM phase. Therefore, the existence of magnetization anisotropy does not affect our argument for the cause of the observed anomalous AMR.

The magnetic domain structures were imaged by means of Lorentzian transmission electron microscopy (TEM) (Hitachi HF-3000L) equipped with a cold-field emission gun and operated at an acceleration voltage of 300 kV. The microscope was equipped with a custom-made objective lens, making the magnetic field almost zero at the sample position. Electron-transparent thin samples were sliced from the same crystal for the AMR measurements and prepared by mechanical polishing and subsequent argon-ion thinning with an acceleration voltage of 4 kV at room temperature. In Lorentzian TEM observations, we used the Foucault mode (Fig. 4 *A* and *B*). In this mode, the incident beam is split by Lorentzian forces with different directions at the diffraction plane. In the case of the 180° magnetic domains, antiparallel magnetic domains produce two spots at the diffraction plane. When only one of the spots is selected by the objective aperture to form an in-focused image, the image with white/black band-shape areas is observed in the in-focused plane. These white/black areas correspond to antiparallel magnetic domains, and domain walls are imaged as a boundary between the white and black areas.

Two-Component Model. To include the effect of twinning existing in the square-rod sample, we realized that the sample has a mixture of twinning domains with their c-axis perpendicular to each other (see Fig. 7) and, as a result, is no longer uniaxial. We considered a simple two-component scenario—one has the ***c***-axis along the *y* direction with a twinning portion δ (minor component), whereas the other is along the *z* direction with a twinning portion $(1 - \delta)$ (major component), and each component has the same prolate ellipsoid dependency as we used for the slab sample. The resistivity-field relation for the minor component, with its ***c***-axis in the *y* direction, is then given by a prolate in the *y* direction:

$$\left(\frac{\rho}{\rho_\perp}\right)^2 \cos^2\Theta + \left(\frac{\rho}{\rho_\perp}\right)^2 \sin^2\Theta\cos^2\Phi + \left(\frac{\rho}{\rho_{//}}\right)^2 \sin^2\Theta\sin^2\Phi = 1.$$

When mixed with the major component (Equation (1)), while preserving the ellipsoid shape, we got the superposition of two perpendicular prolate ellipsoids:

$$\rho = \rho(\Theta, \Phi) = \left(\frac{\cos^2\Theta}{\rho_h^2} + \frac{\sin^2\Theta\sin^2\Phi}{\rho_l^2} + \frac{\sin^2\Theta\cos^2\Phi}{\rho_\perp^2}\right)^{-1/2}$$

where

$$\rho_h^2 = \frac{\rho_{//}^2\rho_\perp^2}{(1-\delta)\rho_\perp^2 + \delta\rho_{//}^2},$$

and

$$\rho_l^2 = \frac{\rho_{//}^2\rho_\perp^2}{\delta\rho_\perp^2 + (1-\delta)\rho_{//}^2}.$$

ρ_h and ρ_l are the resistivities as the ***H*** field is along the major and minor component's ***c***-axis, respectively, whereas $\rho_\perp$ is the resistivity when the ***H*** field is perpendicular to both the major and minor ***c***-axis (or *yz* plane). This two-component model can account for the loss of uniaxial property in the square-rod sample. In addition, we can obtain the parameter δ, the portion of the minor component, by fitting the results from AMR measurements to the proposed two-component model. The result is shown in the *Inset* of Fig. 5*D*. The value found is ~0.4 for the temperature range around the maximum AMR signals, which shows that this two-component model can adequately account for the experimental results of the square-rod sample.

ACKNOWLEDGMENTS. We thank Hongjun Liu and Hao Sha for their technical assistance. We acknowledge financial support from the Chinese Academy of Sciences, National Natural Science Foundation of China, State Key Project of Fundamental Research of China, the Zhejiang Natural Science Foundation (China), MEXT of Japan, and the U.S. National Science Foundation through grant DMR-0346826 (USA).

1. Dagotto E (2005) Complexity in strongly correlated electron systems. *Science* 309:257–262.
2. Tokura Y (2006) Critical features of colossal magnetoresistive manganites. *Rep Prog Phys* 69:797–851.
3. Von Helmolt R, Wecker J, Holzapfel B, Schultz L, Samwer K (1993) Giant negative magnetoresistance in perovskitelike $La_{2/3}Ba_{1/3}MnO_3$. *Phys Rev Lett* 71:2331–2334.
4. Asamitsu A, Tomioka Y, Kuwahara H, Tokura Y (1997) Current switching of resistive states in magnetoresistive manganites. *Nature* 388:50–52.
5. Moritomo Y, Kuwahara H, Tomioka Y, Tokuar Y (1997) Pressure effects on charge-ordering transitions in perovskite manganites. *Phys Rev* B 55:7549–7556.
6. Ahn CH, et al. (2006) Electrostatic modification of novel materials. *Rev Mod Phys* 78:1185–1212.
7. Thomson W (1857) On the electro-dynamic qualities of metals: Effects of magnetization on the electric conductivity of nickel and iron. *Proc R Soc London* 8:546–550.
8. McGuire TR, Potter RI (1975) Anisotropic magnetoresistance in ferromagnetic 3d alloys. *IEEE Trans Mag* MAG-11:1018–1037.
9. Eckstein JN, Bozovic I, O'Donnell J, Onellion M, Rzchowski MS (1996) Anisotropic magnetoresistance in tetragonal La1-*x*CaxMnOδ thin films. *Appl Phys Lett* 69:1312–1314.
10. Ziese M, Sena SP (1998) Anisotropic magnetoresistance of $La_{0.7}Ca_{0.3}MnO_3$ films. *J Phys Condens Matter* 10:2727–2737.
11. O'Donnell J, Eckstein JN, Rzchowski MS (2000) Temperature and magnetic field dependent transport anisotropies in $La_{0.7}Ca_{0.3}MnO_3$. *Appl Phys Lett* 76:218–220.
12. Li Q, Wang HS, Hu YF, Wertz E (2000) Anomalous anisotropic magnetoresistance in $Pr_{0.67}Sr_{0.33}MnO_3$ thin films. *J Appl Phys* 87:5573–5575.
13. Egilmez M, Petterson R, Chow KH, Jung J (2007) Magnetoresistive anisotropy and magnetoresistivity in strained $La_{0.65}Ca_{0.35}MnO_3$ films near the metal-insulator transition. *Appl Phys Lett* 90:232506.
14. Yau JB, et al. (2007) Anisotropic magnetoresistance in colossal magnetoresistive $La_{1-x}Sr_xMnO_3$ thin films. *J Appl Phys* 102:103901.
15. Radaelli PG, et al. (1997) Structural effects on the magnetic and transport properties of perovskite $A_{1-x}A_xMnO_3$ (x = 0.25, 0.30). *Phys Rev B* 56:8265–8276.
16. Huang Q, et al. (1998) Structure and magnetic order in $La_{1-x}Ca_xMnO_3$ ($0 \le x \le 0.33$). *Phys Rev B* 58:2684.
17. Millis AJ, Littlewood PB, Shraiman BI (1995) Double exchange alone does not explain the resistivity of $La_{1-x}Sr_xMnO_3$. *Phys Rev Lett* 74:5144–5147.
18. Zener C (1951) Interaction between the *d*-shells in the transition metals. II. Ferromagnetic compounds of manganese with perovskite structure. *Phys Rev* 82:403–405.
19. Anderson PW, Hasegawa H (1955) Considerations on double exchange. *Phys Rev* 100:675.
20. Kuwahara H, Tomioka Y, Asamitsu A, Moritomo Y, and Tokura Y (1995) A first-order phase transition induced by a magnetic field. *Science* 270:961–963.
21. Tomioka Y, Asamitsu A, Kawahara H, Moritomo Y, and Tokura Y (1996) Magnetic-field-induced metal-insulator phenomena in $Pr_{1-x}Ca_xMnO_3$ with controlled charge-ordering instability. *Phys Rev B* 53:R1689–R1692.
22. Asamitsu A, Moritomo Y, Kumai R, Tomioka Y, Tokura Y (1996) Magnetostructural phase transitions in $La_{1-x}Sr_xMnO_3$ with controlled carrier density. *Phys Rev B* 54:1716–1723.
23. Grundy PJ, Tebble RS (1968) Lorentz electron microscopy. *Adv Phys* 17:153–242.